Applied Acoustics 172 (2021) 107593

Contents lists available at ScienceDirect

Applied Acoustics

journal homepage: www.elsevier.com/locate/apacoust

Low-frequency sound absorption of a metamaterial with symmetrical-coiled-up spaces

Gildean do N. Almeida *, Erasmo F. Vergara *, Leandro R. Barbosa, Ricardo Brum

Graduate Program in Mechanical Engineering, Laboratory of Vibrations and Acoustics, Federal University of Santa Catarina, Florianópolis, Brazil

ARTICLE INFO

Article history:
Received 15 February 2020
Received in revised form 29 June 2020
Accepted 10 August 2020

Keywords:
Low-frequency sound absorption
Acoustic metamaterial
Subwavelength absorber
Symmetrical labyrinth

ABSTRACT

A theoretical, numerical and experimental investigation of a low-frequency acoustic absorber (100–600 Hz) is reported herein. The acoustic metamaterial is based on a micro-perforated panel coupled to a multi-cavity of coiled-up spaces that is similar to a symmetrical labyrinth. On considering the visco-thermal losses, the effect of increasing the number of symmetrically coiled-up spaces that determines the peak position of the sound absorption and allows a greater sound energy absorption is discussed theoretically and proven through numerical analysis (FEM). Prototypes were manufactured using 3D printing technology and evaluated in an impedance tube. The results for the sound absorption coefficient acquired in the desired frequency range were greater than 91% with relative bandwidth above 35%, in agreement with the analytical model. Therefore, it is demonstrated that the proposed absorber presents a scale of deep-subwavelength since its total thickness is 0.033λ.

1. Introduction

In the past two decades, the search for sound energy control in the most diverse everyday situations has motivated the research and development of new acoustic materials. In general, a variety of acoustic devices are used to acquire this control. Notable examples in this broad category are porous materials (e.g., cellular, fibrous and granular) and resonant devices, such as micro-perforated panels (MPP). However, the aforementioned porous materials present excellent sound absorption in the region of medium and high frequencies and low sound absorption in the region of low frequencies, since these materials require dimensions comparable to the operation wavelength [1,2,32]. On the other hand, MPP is a solution for the control of sound energy related to low frequencies, although these types of panels require an air cavity with large physical dimensions [3–6], which is not always possible in practice.

Alternatives for energy control associated with low frequencies (100–600 Hz) that have emerged recently are the acoustic metamaterials or metasurfaces, with enormous potential for application [7–13]. We consider metamaterials as periodic structures that present unique properties and behaviors for long wavelengths [14]. This unique behavior occurs when the metamaterial presents a total surface impedance corresponding to the impedance of the medium, allowing the sound wave to pass efficiently into its interior [10]. In order to design a metamaterial efficiently, the visco-thermal characteristics, which affect the sound propagation in small spaces [15–17], as well as the concept of coiled-up spaces [18,19,33,34] have been found to be very useful. The concept of coiled-up spaces reduces the physical volume of the model to a deep-subwavelength scale and have been widely used in absorber based on Fabry-Pérot (FP) type channels [20,21].

Considering the concept of coiled-up spaces [21] and based on the design of micro-perforated panels [9,10,22], the aim of this study was to design and evaluate the behavior of an absorber metamaterial that occupies a small physical volume. The model is based on a micro-perforated panel coupled to a multi-cavity of coiled-up spaces, similar to a symmetrical labyrinth. The sensitivity analysis is conducted to determine the influence of the geometric parameters on the absorber behavior in the frequency range of 100 - 600 Hz. Lastly, numerical simulations using the finite elements method (FEM) and experimental evaluations in an impedance tube, applying the method of transfer functions to obtain the sound absorption coefficient of two proposed samples, are used to verify that good sound absorption, with broad bandwidth at low frequencies, is acquired.

2. Theoretical and numeric method

The sound absorber was comprised of a rigid panel containing a slit-type micro-perforation located in its geometrical center

* Corresponding authors.
E-mail addresses: gildean_fsa@hotmail.com (G.d.N. Almeida), e.f.vergara@usfc.br (E.F. Vergara).

https://doi.org/10.1016/j.apacoust.2020.107593
0003-682X/

coupled to a multi-cavity of coiled-up spaces. Thus, the sound wave will propagate within the multi-cavity through an allowed double path of propagation. A unit cell with five coiled-up spaces composed of rigid walls and a top view of the unit cell are shown in Fig. 1a) and 1 b), respectively. The geometric parameters considered in the model are defined in the figure.

2.1. Theoretical method

A plane wave of amplitude P is focused on the panel along the x direction. Considering that the model has five coiled-up spaces and the wavelengths are greater than the width of the symmetrical spaces, the wave propagates in the absence of a cutoff frequency [21,23] (see Fig. 1b)), since with the increase in the number of spaces in both directions of the y-axis there is a greater effective length of propagation (L_{eff}) in both directions.

Considering the single coiled-up spaces option, i.e., a single labyrinth, the impedance of total surface (Z_{T_1}) will be given by the series association of the front panel impedance (Z_p) with the impedance of the single space (Z_{e_1}). This is represented by Eq. (1):

$$Z_{T_1} = Z_p + Z_{e_1}. \tag{1}$$

However, the proposed model presents a double coiled-up spaces of the same cross-section area coupled to a single panel. Thus, the total impedance of the model (Z_{glv}) is obtained through the parallel association of the total impedance of a single coiled-up space. This is determined by Eq. (2),

$$Z_{glv} = \frac{Z_{T_1} \times Z_{T_2}}{Z_{T_1} + Z_{T_2}} = \frac{(Z_p + Z_{e_1}) \times (Z_p + Z_{e_2})}{(Z_p + Z_{e_1}) + (Z_p + Z_{e_2})}. \tag{2}$$

The propagation of sound waves in spaces with a constant rectangular cross-sectional area can be described using the complex density and compressibility functions [24]. The acoustic impedance in spaces is represented by a fluid model equivalent and assuming that plane waves propagate in the symmetrical labyrinth, these two functions are obtained by Eqs. (3) and (4), respectively,

$$\rho_{eq} = \rho_o \frac{v a^2 W^2}{4 j\omega} \left[\sum_{k=0}^{\infty} \sum_{n=0}^{\infty} \left[\alpha_k^2 \beta_n^2 \left(\alpha_k^2 + \beta_n^2 + \frac{j\omega}{v} \right) \right]^{-1} \right]^{-1}, \tag{3}$$

$$C_{eq} = \frac{1}{P_o} \left[1 - \frac{4 j\omega(\gamma - 1)}{v' a^2 W^2} \sum_{k=0}^{\infty} \sum_{n=0}^{\infty} \left[\alpha_k^2 \beta_n^2 \left(\alpha_k^2 + \beta_n^2 + \frac{j\omega\gamma}{v'} \right) \right]^{-1} \right], \tag{4}$$

where $\alpha_k = (k + 1/2)\pi/a$ and $\beta_n = (n + 1/2)\pi/W$ are constants and $v' = \kappa/\rho_o C_v$, with $\kappa = 0.026$ W/(m·K) and $C_v = 0.712$ kJ/(kg·K) representing the thermal conductivity and specific heat at constant volume, respectively; $v = \eta/\rho_o$ is the kinematic viscosity of the air, with η = 1.8134 x 10^{-5} Pa·s representing the viscosity of air; $P_o = 101325$ Pa the atmospheric pressure; and $\gamma = 1.41$ the specific heat ratio. From the density and the compressibility functions, it is possible to determine the characteristic impedance $Z_e^c = \sqrt{\rho_{eq}/C_{eq}}$ and the effective acoustic propagation constant $m_{eq} = \omega\sqrt{\rho_{eq} C_{eq}}$ in the double coiled-up spaces [24].

Consequently, the individual acoustic impedance of the coiled-up spaces is obtained through Eq. (5),

$$Z_{e_1} = Z_{e_2} = -j \frac{S_o}{S_i} Z_e^c \cot(m_{eq} L_{eff}), \tag{5}$$

where $S_o = mL$ is the area in the yz plane of an unit cell, $Si = aW$ the cross-section area of the spaces, $a = ((m - b_o) - (n - 1)b_o)/n$, with n representing the number of coiled-up spaces, this will always be an odd number because the proposed model is symmetric, $W = (L - b_o)$, and finally, $L_{eff} \approx ((n - 1)(\sqrt{h^2 + a^2})/2 + h + \psi)$, where $\psi \approx 22$ mm is an average factor for correction of the effective length of propagation. The ratio between areas in Eq. (5) can be understood as an area modifier factor that maintains the conservation of the volume velocity flow.

The panel of the model has a thickness t and has a micro-perforation, i.e., a micro slit, with the height (L_f) being greater than the width (d_f) (see Fig. 1a)). In this case, it can be approximated to an ellipse through the use of the hyperbolic tangent function. Although the micro slit has low acoustic resistance and the end correction for larger mass reactance [22], the choice of the perforation pattern is to obtain a non-typical pattern, where the slits are connected to larger openings allowing greater dissipation of sound energy.

The impedance of a slit was first studied by Lord Rayleigh and later expanded for analysis at low frequencies [25]. However, considering that $L_f \gg d_f$, a new solution and the respective corrections were proposed [22]. The solution of the wave equation for the slit with an axial velocity (x-axis) is obtained using Eq. (6) [22,26],

$$j\omega\rho_o v = \frac{\eta}{y} \frac{\partial}{\partial y} \left(y \frac{\partial v}{\partial y} \right) + \frac{\Delta P}{t}, \tag{6}$$

where v is the particle speed along the x axis and ΔP is the sound pressure drop at the end of the slit. Assuming that the walls are rigid, determining the solution of Eq. (6) and averaging the velocity of particles along the entire slit, Eq. (7) is obtained,

$$\bar{v} = -\frac{1}{j\omega\rho_o} \frac{\Delta P}{t} \left[1 - \frac{\tanh(\sigma\sqrt{j})}{\sigma\sqrt{j}} \right], \tag{7}$$

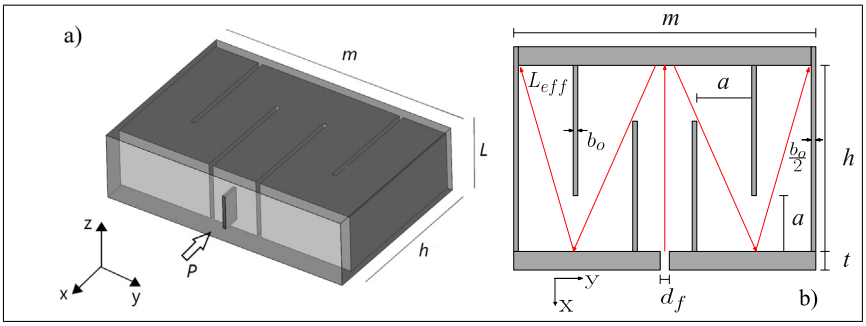

Fig. 1. Structure of acoustic metamaterial with double coiled-up spaces: a) Unitary cell and b) section view of a unit cell in the xy plane. The geometric parameters considered in the model are: the width of the slit on the y-axis (d_f); height on the z-axis (L_f); thickness of the panel and of the air cavity (t, h), respectively; and height and width of a single cell (L, m), respectively. The position of the micro slit along the yz plane is marked by (T), the heigth and width of the cross-section of the coiled-up spaces are (W, a), respectively. The coiled-up space is formed by rigid walls with thickness bo.

where $\sigma = d_f\sqrt{\frac{\rho_o\omega}{4\eta}}$ is the perforation constant [35]. From the velocity of the particles, it is possible to calculate the exact impedance of the panel. For this it is considered that the velocity of the particles in and out of the slit are related by the porosity of the panel, i.e., $v = \Theta\bar{v}$, so the impedance of the panel is obtained by Eq. (8),

$$Z_p = -\frac{\Delta P}{v} = \frac{j\omega\rho_o t}{\Theta}\left[1 - \frac{\tanh(\sigma\sqrt{j})}{\sigma\sqrt{j}}\right]^{-1}, \quad (8)$$

where $\Theta = (d_f L_f)/(mL)$ is the porosity or filling fraction of the slit embedded in the panel.

The air movement at the face of the panel should be compressed in the slit, since its volume is smaller, and this induces a resistance, i.e., $R_{res} = \sqrt{2}\eta\sigma/\Theta d_f = \sqrt{2\rho_o\eta\omega}/2\Theta$ [27,28]. Moreover, based on Rayleigh's derivation for an elliptic aperture, and using an elliptic integral of the first species [22], a final correction for the reactance needs to be defined, due to sound radiation at both ends of the slit [9], i.e., $R_{rea} = (j\omega\rho_o d_f F_e)/(2F(\epsilon)\Theta)$, where $F(\epsilon) = [1 - 1,4\epsilon + 0,338\epsilon^3 + 0,0679\epsilon^5 \ldots]^{-1}$ is the Fok correction function due to the interaction of radiation of the air [28,36], $\epsilon = d_f/L$, and F_e denotes the complete elliptic integral in which an appropriately shaped ellipse approaches the slit, which is obtained by Eq. (9) [22],

$$F_e = \int_0^{\frac{\pi}{2}} \frac{d\theta}{\sqrt{1 - e^2\sin^2\theta}}, \quad (9)$$

where $e = \sqrt{1 - (d_f/2L_f)^2}$ is the eccentricity of the ellipse. In accordance with [22], the exact impedance of the panel with a micro slit and its final corrections is then obtained through Eq. (10)

$$Z_p = \frac{j\omega\rho_o t}{\Theta}\left[1 - \frac{\tanh(\sigma\sqrt{j})}{\sigma\sqrt{j}}\right]^{-1} + \frac{\sqrt{2\rho_o\eta\omega}}{2\Theta} + j\omega\rho_o\frac{F_e d_f}{2F(\epsilon)\Theta}. \quad (10)$$

After some simplifications the real and imaginary part of the approximate impedance of the panel with a micro slit is given by Eq. (11),

$$Z_p = \frac{12\eta t}{\Theta d_f^2}\left(\sqrt{1 + \frac{\sigma^2}{18}} + \frac{\sqrt{2}\sigma d_f}{12h}\right) + \frac{j\rho_o\omega t}{\Theta}\left[1 + \frac{1}{\sqrt{5^2 + 2\sigma^2}} + \frac{F_e d_f}{2tF(\epsilon)}\right]. \quad (11)$$

By substituting Eqs. (10) and (5) in Eq. (2) one arrives at the equation for the total impedance of the proposed acoustic metamaterial. Considering normal wave incidence, the sound absorption coefficient of the absorber with rigid backing can be obtained by Eq. (12),

$$\alpha = 1 - \left|\frac{Z_{glv}/Z_o - 1}{Z_{glv}/Z_o + 1}\right|^2, \quad (12)$$

where $Z_o = \rho_o c_o$ is the characteristic air impedance, in which $\rho_o = 1.21$ kg.m^{-3} and $c_o = 343$ m.s^{-1} are the density and speed of sound in air, respectively.

2.2. Numerical analysis by FEM

A numerical validation of the proposed absorber was performed using the software COMSOL Multiphysics with the finite element method (FEM). Visco-thermal losses in the micro-slit and the coiled-up spaces (mainly as they increase symmetrically) are accounted for using the Thermoacoustic module. However, because the samples of the acoustic metamaterial were manufactured by the 3D printing technology using ABS material, in the numerical validation it was assumed that there is no fluid–structure interaction because all of the walls of the structure are considered acoustically rigid perfect bodies, since ABS has a density and speed of sound higher than air ($\rho = 1180$ kg.m^{-2}; $c = 2700$ m.s^{-1}). A limit condition of plane wave radiation was used to simulate the incidence of the sound waves in the model. The mesh size of the elements was chosen using the Nyquist criteria, so that the visco-thermal dissipations, especially in the narrow regions, were captured in the simulation. The element type selected was the free tetrahedral and the minimum element size was defined as 1/10 of the smallest simulated wavelength.

3. Results and discussions

3.1. Theoretical model analysis

The theoretical analysis of the behavior of the acoustic absorber was carried out with the implementation of the sound absorption coefficient and the total surface impedance of different unit cells, as shown in Fig. 2. The geometric parameters used in the following analysis are shown in Table 1. The value of the elliptic integral (F_e) is 5.6 (meaning that the slit used to approach the ellipse has a very high largest to smallest parameter ratio) and the correction due to the interaction of the air radiation in the panel slit ($F(\epsilon)$) is 1, since the panel presents only one perforation, and, therefore, there is no interaction between perforations.

Fig. 3 shows the behavior of the absorption coefficient of the model for different cells. The sound absorption peaks are located at 344 Hz, 313 Hz, 279 Hz and 248 Hz for n = 5, 7, 9 and 11 coiled-up spaces, respectively. Thus, it can be observed that the peak of sound absorption moves to lower frequencies as the value of n increases. Furthermore, the absorption peaks have amplitudes of 1.00, 0.99, 0.99 and 0.99 and the relative bandwidths at 50% of the maximum absorption are 206 Hz, 139 Hz, 95 Hz and 67 Hz for n = 5, 7, 9 and 11, respectively. Consequently, the values for the relationship between the bandwidth and the center frequency are 60.0%, 44.5%, 34.0% and 27.0%, respectively.

It can be seen in Fig. 3 that the absorber presents broadband absorption, which demonstrates that the concept of double coiled-up spaces increases the capacity of the model to absorb a greater amount of sound energy, although this bandwidth decreases as n increases. However, part of this energy is dissipated, initially in the slit region due to viscous friction [9] and then in the coiled-up spaces when these increase due to the visco-thermal effects. Moreover, with an increase in n the cross-sectional area of these spaces (S_i) decreases and, consequently, the peaks of the sound absorption move strongly to low frequencies due to two factors: firstly, the greater influence of the visco-thermal effects; and secondly, an increase in the effective propagation length (L_{eff}) since, as detailed below, this length plays an important role in the frequency of operation of the absorber [21,29].

The double coiled-up spaces can be simplified as a Fabry-Pérot-like (FP) channel (FP) [30], since both L_{eff} and S_i affect the position of the peak sound absorption. Fig. 4 illustrates the influence of S_i on the behavior of the absorber when S_i varies with $L_{eff} = 202.8$mm. The frequency of the peak absorption increases as S_i decreases, i.e., a smaller cross-sectional area of the coiled-up spaces induces absorption at higher frequencies, which is the opposite effect compared with the parameter L_{eff}. Therefore, the operation frequency of the absorber is mainly determined by L_{eff}, which can be adjusted to the required frequency by modifying the value of n or the parameter h.

The sound absorption performance of the metamaterial is related to the behavior of its total surface impedance (Z_{glv}). Thus, good agreement with the air impedance, total sound absorption

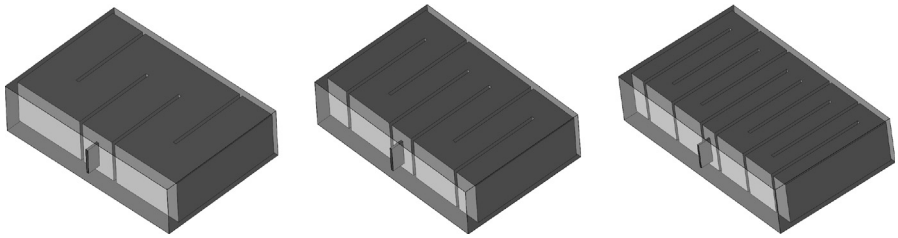

Fig. 2. Configurations of the symmetrical labyrinth metamaterial, with 5, 7 and 11 coiled-up spaces, respectively.

Table 1
Parameters (in units of mm) used and calculated in the analysis of individual cells.

Geometrical parameters	d_f	L_f	m	h	b_o	L	t
Value	0.38	13.0	45.0	36.0	1.0	16.0	2.4
Calculated parameters	n= 5	n = 7	n = 9	n = 11			
a (space cross-sectional width) [mm]	8.0	5.43	4.0	3.1			
L_{eff} (effective propagation length) [mm]	131.7	167.2	202.8	238.7			

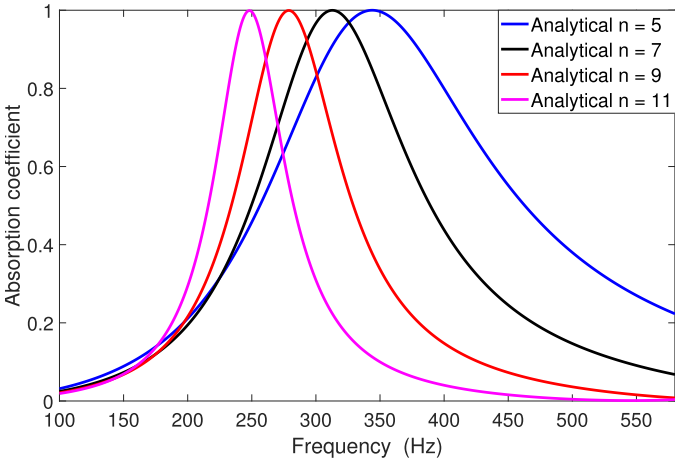

Fig. 3. Sound absorption coefficient of different model configurations.

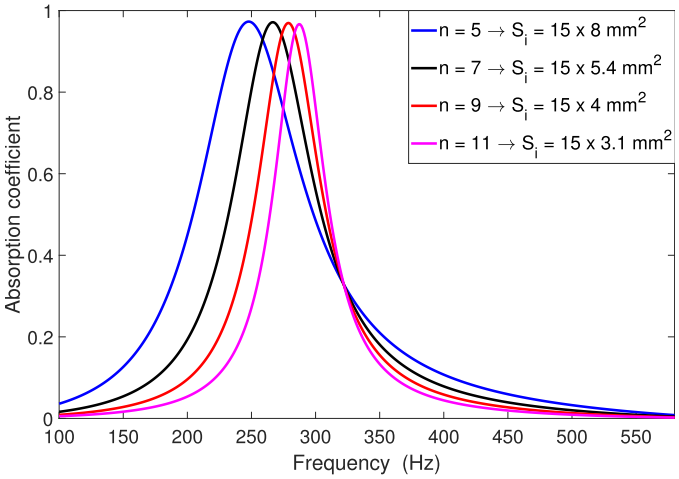

Fig. 4. Sound absorption coefficient for variations in S_i and fixed L_{eff}.

is obtained, which means that $Re(Z_{glv}/Z_o = 1)$ and $Im(Z_{glv}/Z_o = 0)$. The total normalized surface impedance by the air impedance is represented in Fig. 5. The real parts are 0.98, 0.97, 0.95 and 0.94 at peak absorptions of 344 Hz, 313 Hz, 279 Hz and 248 Hz, respectively. Meanwhile, the imaginary parts are zero for these same frequencies. The total sound absorption is almost achieved when $n = 5$, at which real part is closer to the unitary value, demonstrating an approximately optimal adjustment of the total surface impedance of the absorber in this medium.

It can also be seen in Fig. 5 that as n increases the curves of the real part of the impedance tend to move further apart above the unit value and closer together below this value. Furthermore, the curves of the imaginary part above zero increase with an increase in n and below zero tend to approximate and decay, which means that in these regions the model does not act efficiently.

3.2. FEM simulation

Numerical validation was conducted using the same geometric parameters (Table 1). The values obtained for the sound absorption coefficient with the analytical and numerical methods are shown in Fig. 6. A good agreement between the methods is verified, mainly when the number of coiled-up spaces of the absorber increases symmetrically. This cohesion is due to the greater influence of the effects of viscous friction and thermal diffusion in these spaces, since the cross-sectional area of these spaces decreases with an increase in n. The displacement of the sound absorption peak to lower frequencies is corroborated by the numerical analysis. This is due to the high level of resonance produced by the strong compression of the air in the micro slit of the panel, promoting dissipation of the energy due to of friction losses and viscous damping both in the perforation and inside the symmetrical coiled-up spaces [21]. The point of distinction between the methods occurs in the bandwidth relative to 50% of the maximum absorption, mainly for the cell with $n = 5$ coiled-up spaces, where the bandwith is $\Delta f = 206$ Hz and $\Delta f = 178$ Hz for the analytical and numerical methods, respectively which characterizes a relative error of 13.6%. Concerning the amplitude, the maximum error found was 3.0% relative to $n = 11$ coiled-up spaces.

To further explore and comprehend the low-frequency sound absorption mechanism of the acoustic metamaterial, we plotted the acoustic pressure field at the resonance frequency of the unit cells with $n = 5$ and 11 coiled-up spaces in Fig. 7. It can be seen that the sound pressure at the end of the symmetrical coiled-up spaces is three and eight times higher than at the entrance (micro slit). As a result, the incident of the wave energy is mainly dissipated due to the greater friction between the acoustic wave and the small perforation. Therefore, the main low-frequency absorp-

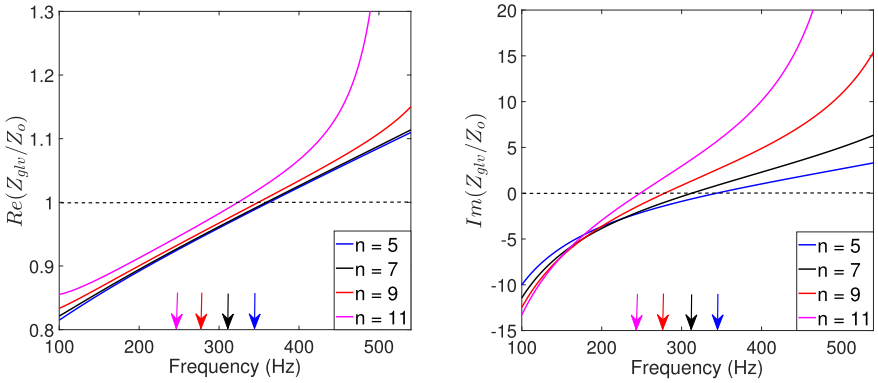

Fig. 5. Total normalized surface impedance behavior of the model.

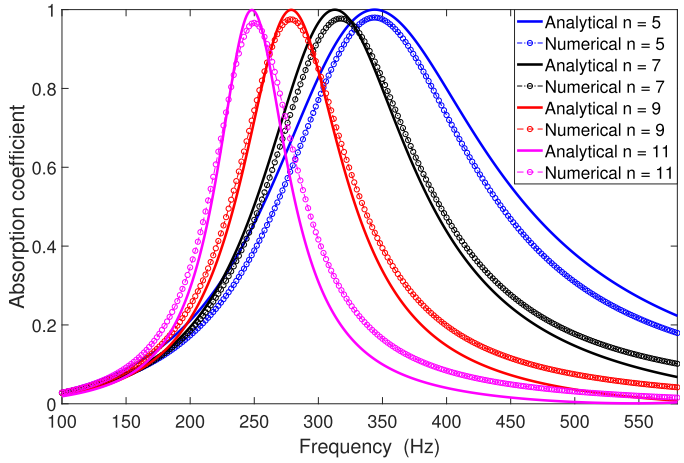

Fig. 6. Sound absorption coeffcient results (analytical and numerical methods) for the absorber.

tion mechanism of the acoustic absorber is the conversion of acoustic energy into heat energy at the resonance frequency.

As verified above, only a single absorption peak at a low frequency with broadband can be obtained by the absorber studied. However, when it is necessary to further extend the relative absorption bandwidth a strategy that can be adopted is the parallel coupling of different unit cells with different parameters. Therefore, the new impedance is obtained using the Eq. (13),

$$\frac{1}{Z_{ac}} = \frac{1}{S_o}\sum_{i=1}^{N}\frac{S_{oi}}{Z_{glv}} \tag{13}$$

where N is the number of coupled unit cells, $S_o = \sum_{i=1}^{N} S_{oi}$, with S_{oi} the area of each cell and Z_{ac} the impedance of the coupled system.

Fig. 8 shows the sound absorption coefficient results, obtained applying the analytical (black line) and numerical (pink line) methods, for the absorber with two different cells coupled. The geometric paramaters used in the evaluation are given in the legend of the figure. For comparison, the sound absorption curve for the unit cells is also displayed (dashed red and blue lines). One can observe two peaks in the sound absorption, at 303 Hz and 389 Hz for the analytical method and 312 Hz and 387 Hz for numerical method. These peaks do not coincide with individual peaks due to the influence of the coupling processes [21]. The absorption peaks of the coupled system have smaller amplitude, due to the overlapping of the effects resulting from the different cells, which suppresses the amplitude of the sound absorption of the coupled system [37]. However, both peaks have amplitudes over 90% and combine into a broadband absorption with a relative width of up to 49.5%.

3.3. Sensitivity analysis

Based on Eqs. (5) and (10), it can be concluded that the behavior of the sound absorption coefficient of acoustic metamaterial is mainly dependent on five geometric parameters (d_f, L_f, h, m, t). The influence these parameters was investigated for a unit cell with $n = 5$ coiled-up spaces, since for the other configurations the behavior was similar. The fixed parameters in the analysis were those listed in Table 1 and the parameter to be varied is shown on the vertical axis of each figure.

The slit width varied from 0.3 mm to 1.1 mm and Fig. 9 a) shows that the absorber presents maximum sound absorption when the parameter values are between 0.3 mm and 0.45 mm and that above these values the amplitude of absorber is attenuated. Furthermore, with increases in the geometric parameter, the sound absorption curve moves gradually to high frequencies. The slit height was varied from 4 mm to 16 mm and Fig. 9 b) shows that the absorber presents maximum sound absorption when the parameter was varied from $L_f = 10$ mm to its maximum value.

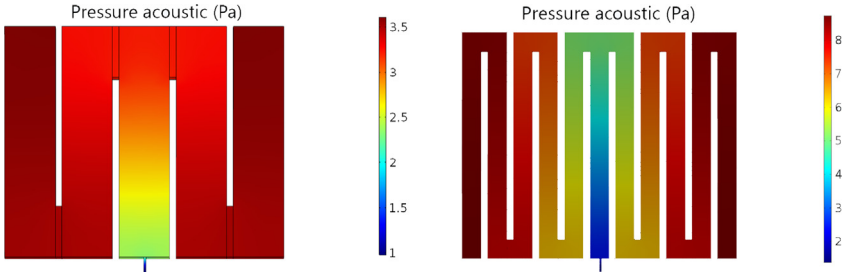

Fig. 7. Sound pressure field of the cells with $n = 5$ and 11 coiled-up spaces at the operating frequencies of 344 Hz and 250 Hz, respectively.

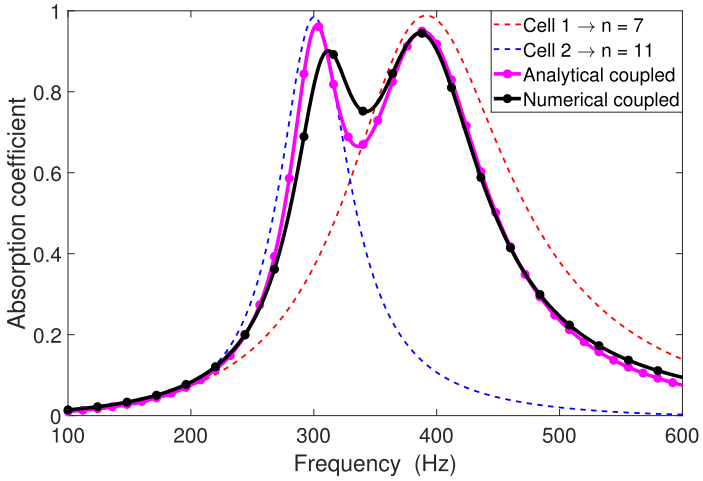

Fig. 8. Behavior of the sound absorption coefficient of the coupled system and the unit cells. The geometric parameters used were: m = 39.0 mm, L = 12.0 mm, d_f = 0.36 mm, L_f = 9.0 mm, h = 30.0 mm, b_o = 1.0 mm and t = 1.5 mm.

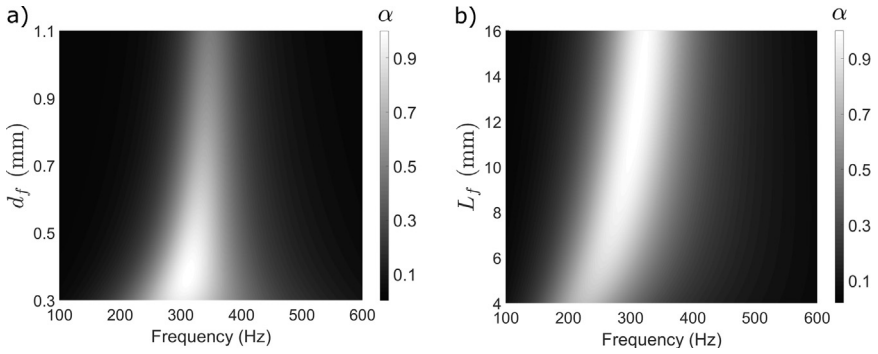

Fig. 9. Behavior of sound absorption coefficient with variations in the parameters d_f and L_f.

However, the sound absorption curve moves to high frequencies with a variation in this parameter. It can be noted that the bandwidth at 50% of the maximum absorption increases as the geometric parameter (L_f) increases, throughout the range.

The thickness of the air cavity was varied from 15 mm to 60 mm and Fig. 10 a) demonstrates that the sound absorption peak shifts strongly to lower frequencies (from 530 Hz to 215 Hz) as the geometric parameter increases, demonstrating that this parameter plays a fundamental role in achieving sound absorption in this frequency region. This influence can be confirmed through the equation that determines the effective length of propagation (L_{eff}), because L_{eff} is proportional to h. In addition, the shifts in the absorption peak to lower frequencies cause only a slight change in the bandwidth at 50% of the maximum absorption. This finding can be understood through the symmetrical coiled-up spaces since these have the capacity to absorb a greater amount of sound energy. Another interpretation for the slight variation in bandwidth is the fact that the cross-sectional area of the coiled-up spaces remains unchanged, since the that arrangement of the coiled spaces is not dependent on the parameter h.

The cell width varied from 30 mm to 70 mm and Fig. 10 b) shows that the peak sound absorption shifts to lower frequencies with increases in this geometric parameter. This shift is due to an increase in the cross-sectional area of the symmetrical

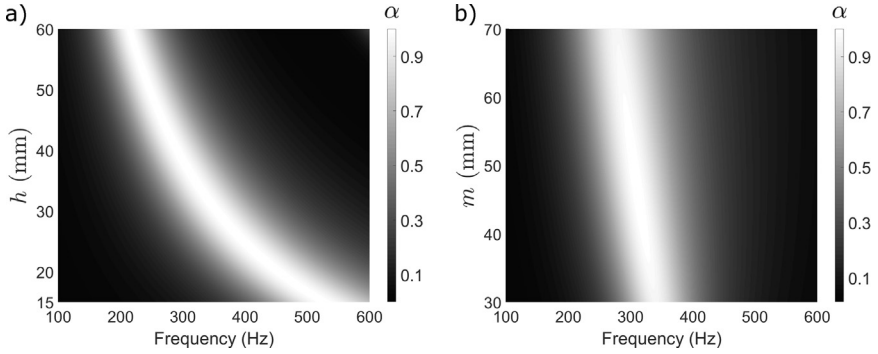

Fig. 10. Behaviour of sound absorption coefficient with variations in the parameters h and m.

coile-up spaces and, consequently, in the volume of fluid and this contributes to an increase in the thermoacoustic losses. Another interpretation of this shift is an increase in L_{eff}.

Lastly, the panel thickness was varied from 1 mm to 6 mm and Fig. 11 demonstrates that the peak sound absorption shifts to lower frequencies with this variation in the geometric parameter.

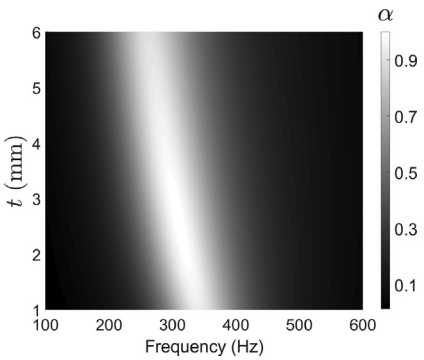

Fig. 11. Behavior of sound absorption coefficient due to parameter *t*.

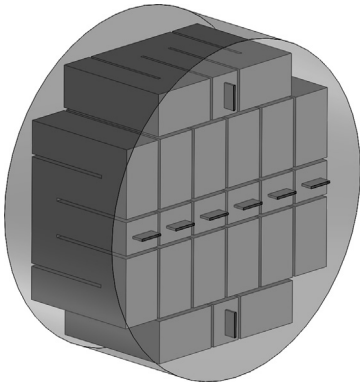

Fig. 12. Structure sketch of sample 1 with 8 cell units for the experiment.

Furthermore, the absorber shows a maximum amplitude in the frequency range of 300 - 340 Hz when the panel thickness values are between 1.5 mm and 3.5 mm.

4. Experimental validation

The sound absorption coefficient of the metamaterial was evaluated using a cylindrical impedance tube with an internal diameter of 107 mm, using the standard two-microphone method [31]. A sample containing unit cells with $n = 5$ coiled-up spaces was produced using the additive manufacturing (3D printing) technology and the fusion and deposition modeling (FDM) technique. Because of its durability, ABS was used to manufacture the absorber. The resolution of manufacture was 0.1 mm. Due to the physical limitation of the impedance tube, sample 1 was manufactured to fit the tube, which limited the number of unit cells to eight (see Fig. 12). The geometrical parameters considered in the manufacture and analysis of the model were acquired from sensitivity analysis and are listed in Table 2.

The results reported in Fig. 13 show the good agreement with the values for the sound absorption coefficient of the sample 1 applying the analytical, numerical and experimental methods. The corresponding sound absorption peaks were determined at 274 Hz, 274 Hz and 285 Hz, respectively. The sound absorption peak amplitudes were 0.97, 0.96 and 0.97, respectively. The discrepancy observed in the frequency values obtained experimentally and with the prediction methods is associated with inaccuracies related to the manufacturing of the sample [9,29], i.e., the roughness of the internal walls of the symmetrical coiled-up spaces, well as the effect of the coupling of the various unit cells.

The values for the bandwidth relative to 50% of the maximum absorption were 127 Hz, 98 Hz and 100 Hz for the analytical, numerical and experimental methods, respectively. The corresponding values for the relationship between the bandwidth and the peak central frequency are 46.3%, 35.7% and 35.0%, respectively. One can see that frequency bandwidth of the experimental result is greater than that of the analytical and numerial methods, probably due to the additional consumption of sound energy by

Table 2
Parameters (in mm) derived from the sensitivity analysis and used to manufacture sample 1.

Geometrical parameters	d_f	t	m	h	b_o	L_f	L
Value	0.7	4.0	58.0	40.0	10	8.0	14.5

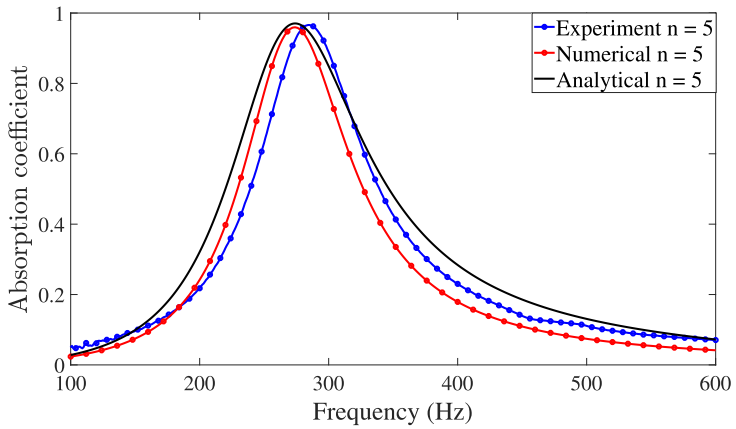

Fig. 13. Theoretical, numerical and experimental behavior of the sound absorption coefficient for sample 1.

the rough surface obtained in the 3D printing [38], which is not considered in the analytical and numerical methods. Thus, based on the experimental bandwidth value and the operation frequency, it can be stated that the acoustic metamaterial acts as a deep-subwavelength absorber [9,17,21], since its total thickness is much smaller than the operation frequency wavelength, $(h + t) \approx 0.033\lambda$.

A second experimental analysis was performed with a sample containing unit cells with $n = 5$ coiled-up spaces. The geometric parameters were proposed from the sensitivity analysis and are listed in Table 3. Fig. 14 shows a sketch of the structure and the printout of sample 2, with the number of unit cells limited to ten.

Fig. 15 reports the sound absorption coefficient results for sample 2 obtained with the analytical, numerical and experimental methods. The corresponding sound absorption peaks were located at 460 Hz, 472 Hz and 488 Hz, respectively. The sound absorption peaks had amplitudes of 0.97, 0.96 and 0.91, respectively. A large discrepancy between the frequency and amplitude values of experimental results and predictioned results is observed. In the case of frequency, we attribute this to inaccuracies related to the sample manufacture while the discrepancy in the amplitude results is related to the area of the cells that fill a smaller cross-sectional area of the impedance tube and also to the uncertainty associated with the sample fabrication. Also, the bandwidths relative to 50% of the maximum absorption were 226 Hz, 167 Hz and 220 Hz for the analytical, numerical and experimental methods, respectively. Therefore, the values for the relationship between the bandwidth and the peak central frequency are 49.0%, 35.4% and 45.0%, respectively. Once again, based on the experimental bandwidth value and the operating frequency of the model, it can be stated that the proposed acoustic metamaterial acts as a deep-subwavelength absorber, since its total thickness is much smaller than the operating frequency wavelength, $(h + t) \approx 0.037\lambda$.

It is important to highlight two important factors of the proposed absorber. One is that because it has symmetrical multiple cavities, that is, double coiled-up spaces, the absorber allows greater absorption of sound energy. However, this symmetry of the cavities makes the adjustment of geometric parameters more laborious. This is important since the adjustment allows an excellent correspondence between the total impedance and the impedance of the medium and, consequently, a total sound absorption

Table 3
Parameters (in mm) derived from the sensitivity analysis and used to manufacture sample 2.

Geometrical parameters	d_f	t	m	h	b_o	L_f	L
Value	0.5	2.2	46.0	240	1.0	90	13.0

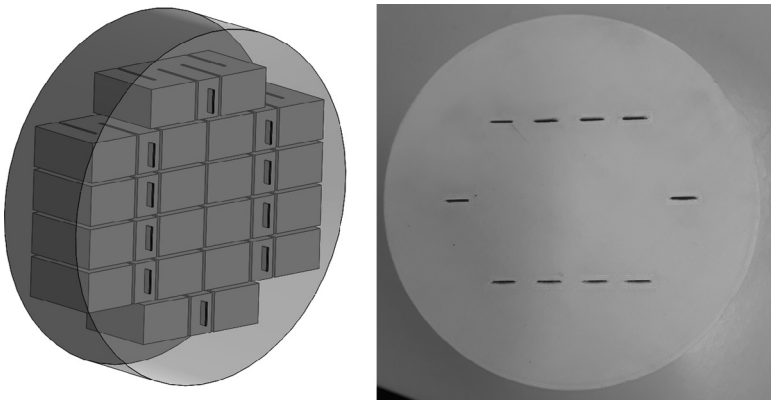

Fig. 14. Sketch of the structure and printout of sample structure 2 with 10 cell units for the experiment.

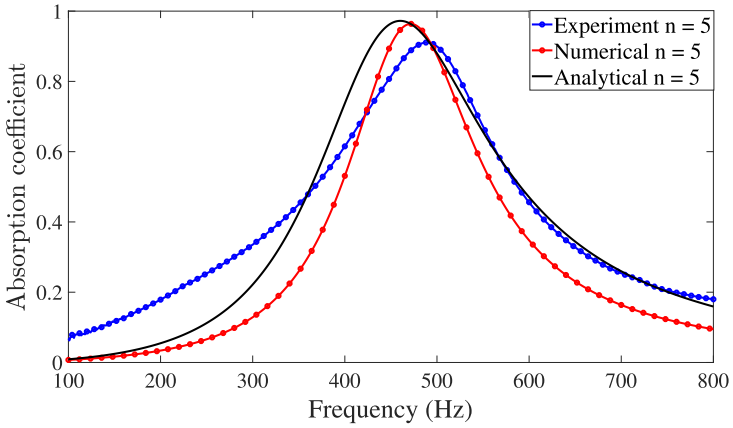

Fig. 15. Theoretical, numerical and experimental behaviour of the sound absorption coefficient for sample 2.

can be obtained. The other important factor of the absorber, as noted in Fig. 3, is that depending on the values of the geometric parameters, the difference in the effective length of propagation (L_{eff}) for the configurations with $n = 5$ and $n = 7$ coiled-up spaces may be small, displaying a small difference between the positions of the sound absorption peaks. Therefore, it is recommended that the thickness of the h air cavity is at least half the width of a m cell, so that the difference in the position between the sound absorption peaks is satisfactory.

5. Conclusions

A metamaterial that is a low-frequency absorber was proposed based on a micro-perforated panel coupled to a multi-cavity of coiled-up spaces. Analytical and numerical (FEM) methods demonstrated good agreement for the sound absorption at low frequencies (100–600 Hz). Through a sensitivity analysis, it was noted that the parameters h and m play an important role in the behavior of the absorber in this frequency range. The sound energy control mechanism was investigated experimentally and found to be in good agreement with the theoretical and numerical methods, mainly for sample 1, although excellent results were also obtained for sample 2. Broadband sound absorption was obtained experimentally, which corroborates the theory that this performance is due to the double spiral spaces, i.e., to the symmetrical labyrinth allowing greater control of the sound energy. Lastly, the sound absorption performance and the ability to adjust the design make the sound absorber an excellent candidate for controlling sound energy in relation to low frequencies. However, the absorber must be manufactured with a sufficiently rigid material, to ensure that there are no structural vibrations at its internal walls, which would affect its performance.

CRediT authorship contribution statement

Gildean do N. Almeida: Conceptualization, Formal analysis, Writing - original draft, Validation. **Erasmo F. Vergara:** Methodology, Writing - review & editing, Formal analysis, Supervision, Funding acquisition. **Leandro R. Barbosa:** Funding acquisition, Validation, Investigation, Writing - review & editing. **Ricardo Brum:** Investigation, Visualization, Data curation, Software.

Declaration of Competing Interest

The authors declare that they have no known competing financial interests or personal relationships that could have appeared to influence the work reported in this paper.

Acknowledgements

The authors are grateful for the financial support for this research provided by the Graduate Program in Mechanical Engineering (POSMEC) and the Laboratory of Vibrations and Acoustics (LVA) of the Federal University of Santa Catarina.

References

[1] Allard J-F, Daigle G. Propagation of sound in porous media: modeling sound absorbing materials. Acoust Soc Am J 1994;95:2785. https://doi.org/10.1121/1.409801.
[2] Bies D, Hansen C. Engineering noise control: theory and practice. New York, NY, USA: Taylor and Francis; 2009.
[3] Maa D-Y. Microperforated-panel wideband absorbers. Noise Control Eng J 1987;29(3):77–84. https://doi.org/10.3397/1.2827694.
[4] Wang C, Huang L, Zhang Y. Oblique incidence sound absorption of parallel arrangement of multiple micro-perforated panel absorbers in a periodic pattern. J Sound Vib 2014;333(25):6828–42. https://doi.org/10.1016/j.jsv.2014.08.009.
[5] Li D, Chang D, Liu B. Enhanced low-to mid-frequency sound absorption using parallel-arranged perforated plates with extended tubes and porous material. Appl Acoust 2017;127:316–23. https://doi.org/10.1016/j.apacoust.2017.06.019.
[6] Bravo T, Maury C, Pinhède C. Optimising the absorption and transmission properties of aircraft microperforated panels. Appl Acoust 2014;79:47–57. https://doi.org/10.1016/j.apacoust.2013.12.009.
[7] Tang Y, Xin F, Huang L, Lu T. Deep subwavelength acoustic metamaterial for low-frequency sound absorption. EPL (Europhys Lett) 2017;118(4):44002. https://doi.org/10.1209/0295-5075/118/44002.
[8] Jung JW, Kim JE, Lee JW. Acoustic metamaterial panel for both fluid passage and broadband soundproofing in the audible frequency range. Appl Phys Lett 2018;112(4). https://doi.org/10.1063/1.5004605. 041903.
[9] Zhao H, Wang Y, Wen J, Lam YW, Umnova O. A slim subwavelength absorber based on coupled microslits. Appl Acoust 2018;142:11–7. https://doi.org/10.1016/j.apacoust.2018.08.004.
[10] Li J, Wang W, Xie Y, Popa B-I, Cummer SA. A sound absorbing metasurface with coupled resonators. Appl Phys Lett 2016;109(9). https://doi.org/10.1063/1.4961671. 091908.
[11] Zhao X, Cai L, Yu D, Lu Z, Wen J. A low frequency acoustic insulator by using the acoustic metasurface to a helmholtz resonator. AIP Adv 2017;7(6). https://doi.org/10.1063/1.4989819. 065211.
[12] Krushynska A, Bosia F, Miniaci M, Pugno N. Spider web-structured labyrinthine acoustic metamaterials for low-frequency sound control. New J Phys 2017;19(10). https://doi.org/10.1088/1367-2630/aa83f3. 105001.
[13] Leblanc A, Lavie A. Three-dimensional-printed membrane-type acoustic metamaterial for low frequency sound attenuation. J Acoust Soc Am 2017;141(6). https://doi.org/10.1121/1.4984623.
[14] Gan WS. New acoustics based on metamaterials, 2018, doi:10.1007/978-981-10-6376-3.
[15] Groby J-P, Huang W, Lardeau A, Aurégan Y. The use of slow waves to design simple sound absorbing materials. J Appl Phys 2015;117(12). https://doi.org/10.1063/1.4915115. 124903.
[16] Jiménez N, Groby J-P, Pagneux V, Romero-García V. Iridescent perfect absorption in critically-coupled acoustic metamaterials using the transfer matrix method. Appl Sci 2017;7(6):618. https://doi.org/10.3390/app7060618.
[17] Jiménez N, Huang W, Romero-García V, Pagneux V, Groby J-P. Ultra-thin metamaterial for perfect and quasi-omnidirectional sound absorption. Appl Phys Lett 2016;109(12). https://doi.org/10.1063/1.4962328. 121902.
[18] Zhang C, Hu X. Three-dimensional single-port labyrinthine acoustic metamaterial: perfect absorption with large bandwidth and tunability. Phys Rev Appl 2016;6(6). https://doi.org/10.1103/PhysRevApplied.6.064025. 064025.
[19] Li Y, Assouar BM. Acoustic metasurface-based perfect absorber with deep subwavelength thickness. Appl Phys Lett 2016;108(6). https://doi.org/10.1063/1.4941338. 063502.
[20] Wu F, Xiao Y, Yu D, Zhao H, Wang Y, Wen J. Low-frequency sound absorption of hybrid absorber based on micro-perforated panel and coiled-up channels. Appl Phys Lett 2019;114(15). https://doi.org/10.1063/1.5090355. 151901.
[21] Wang Y, Zhao H, Yang H, Zhong J, Wen J. A space-coiled acoustic metamaterial with tunable low-frequency sound absorption. EPL (Europhys Lett) 2018;120(5):54001. https://doi.org/10.1209/0295-5075/120/54001.
[22] Dah-You M. Theory of microslit absorbers. Acta Acust 2000;25(6):481–5.
[23] Li Y, Liang B, Gu Z-M, Zou X-Y, Cheng J-C. Unidirectional acoustic transmission through a prism with near-zero refractive index. Appl Phys Lett 2013;103(5). https://doi.org/10.1063/1.4817249. 053505.
[24] Stinson MR. The propagation of plane sound waves in narrow and wide circular tubes, and generalization to uniform tubes of arbitrary cross-sectional shape. J Acoust Soc Am 1991;89(2):550–8. https://doi.org/10.1121/1.400379.
[25] Beranek L, Acoustics M-H. New york; 1954, Reprinted by ASA..
[26] Allard J, Atalla N. Propagation of sound in porous media: modelling sound absorbing materials 2e. John Wiley & Sons 2009. https://doi.org/10.1002/9780470747339.
[27] Cox T, d'Antonio P. Acoustic absorbers and diffusers: theory, design and application. CRC Press 2016. https://doi.org/10.1201/9781315369211.
[28] Cobo P, Simón F. Multiple-layer microperforated panels as sound absorbers in buildings: a review. Buildings 2019;9(2):53. https://doi.org/10.3390/buildings9020053.
[29] Wang Y, Zhao H, Yang H, Zhong J, Zhao D, Lu Z, Wen J. A tunable sound-absorbing metamaterial based on coiled-up space. J Appl Phys 2018;123(18). https://doi.org/10.1063/1.5026022. 185109.
[30] Yang M, Sheng P. Sound absorption structures: from porous media to acoustic metamaterials. Annu Rev Mater Res 2017;47:83–114. https://doi.org/10.1146/annurev-matsci-070616-124032.
[31] Standard B, et al., Acoustics-determination of sound absorption coefficient and impedance in impedance tubes—part 2: Transfer-function method, BS EN ISO; 2001. 10534-2.
[32] S. Xie, D. Wang, Z. Feng, S. Yang. Sound absorption performance of microperforated honeycomb metasurface panels with a combination of multiple orice diameters,. Applied Acoustics 2020;158:107046. https://doi.org/10.1016/j.apacoust.2019.107046.
[33] H. Zhao, Y. Wang, D. Yu, H. Yang, J. Zhong, F. Wu, et al. A double porosity material for low frequency sound absorption,. Composite Structures 2020;239:111978. https://doi.org/10.1016/j.compstruct.2020.111978.

[34] X. Wang, Y. Zhou, J. Zhu. A generalized model for space-coiling resonators. Applied Acoustics 2020;158:107045. https://doi.org/10.1016/j.apacoust.2019.107045.
[35] D.-Y. Maa. Potential of microperforated panel absorber. The Journal of the Acoustical Society of America 1998;104(5):2861–6. https://doi.org/10.1121/1.480 423870.
[36] P. Cobo, C. de la Colina, F. Simón. On the modelling of microslit panel absorbers. Applied Acoustics 2020;159:107118. https://doi.org/10.1016/j.apacoust. 2019.107118.
[37] A. Merkel, G. Theocharis, O. Richoux, V. Romero-García, V. Pagneux. Control of acoustic absorption in one-dimensional scattering by resonant scatterers. Applied Physics Letters 2015;107(24):244102. https://doi.org/10.1063/1.4938121.
[38] S.G. Kandlikar, D. Schmitt, A.L. Carrano, J.B., Taylor. Characteriza- tion of surface roughness eects on pressure drop in single-phase ow in minichannels. Physics of Fluids 2005;17(10):100606. https://doi.org/10.1063/1. 505 1896985.